Bulletin of the Seismological Society of America, Vol. 99, No. 2B, pp. 1162–1173, May 2009, doi: 10.1785/0120080115

Source and Basin Effects on Rotational Ground Motions: Comparison with Translations

by Haijiang Wang, Heiner Igel, František Gallovič, and Alain Cochard

Abstract The recent availability of accurate observations of rotational ground motions has reopened interest in understanding near-fault characteristics of such motions in the context of strong ground motion and earthquake engineering. In order to investigate source and structure-dependent variations of rotational motions, we simulate several *M* 7 earthquakes with varying source scenarios on the Newport–Inglewood (NI) fault embedded in the 3D Los Angeles basin using a finite-difference method in the frequency range up to 0.5 Hz. We use a precalculated database with several hundred numerical Green's functions for a discretized model of the NI fault that allows arbitrary finite-fault scenarios to be synthesized by superposition. We investigate source and basin effects on the rotational part of ground motion (namely maximum peak ground rotation rates and their variations) and compare them with the corresponding values of translational motion. Our main conclusions are: (1) the pure strike-slip source mechanism leads to larger rotation rates around the vertical axis than around the horizontal ones; (2) variation of hypocenter introduces more scatter on ground rotation rate than variations of slip history; (3) the coprocessing of translation and rotation recordings might reveal information on local velocity structure as indicated by plane-wave theory; and (4) the attenuation of accelerations (horizontal components) and rotation rate (vertical component) with distance from the fault are very similar, suggesting that similar expressions (as a function of distance) as for the peak accelerations can be adopted for the peak rotation rates when determining their attenuation relations.

Introduction

In conventional earthquake engineering, seismic loads on structures are formulated only in terms of the three translational ground-motion components. Nevertheless, each site on the surface is subjected to six types of motions: three translations along the x, y, and z axes as well as three rotations about these axes (plus six components of strain in a deformable body). The components of the vector of rotation $\mathbf{\Omega}(\mathbf{x}, t)$ are defined as half the curl of the wave field $\mathbf{u}(\mathbf{x}, t)$ at the surface point $\mathbf{x}$:

$$\mathbf{\Omega}(\mathbf{x}, t) = 1/2\nabla \times \mathbf{u}(\mathbf{x}, t). \quad (1)$$

While the building response to translational motions has been thoroughly investigated, the study of building response to rotational motions is a relatively new field. The engineering importance of rotational components of seismic strong ground motion was noted during the late sixties and early seventies of the last century (e.g., Newmark and Hall, 1969; Newmark and Rosenblueth, 1971). There are many reports about rotations of tombstones and stone lanterns during large earthquakes (e.g., Yamaguchi and Odaka, 1974). Zembaty (2006) also pointed out that rotation effects become especially important in the case of high-rise buildings. Different studies have shown that rotational excitations around horizontal axes can be significant (e.g., Gupta and Trifunac, 1987, 1988, 1989, 1990, 1991). For example, rotational excitations around horizontal axes are important for tall structures supported by soft soil. Excitations around the vertical axis can dominate the response of long and stiff structures supported by soft soils (Zembaty and Boffi, 1994). Such buildings are very sensitive to angular momentum carried by rotational waves. Despite these obvious effects of rotational motions, they are not considered in earthquake engineering.

Theoretical studies (e.g., Boratynski and Teisseyre, 2004; Teisseyre, 2004) and observational results (e.g., Nigbor, 1994; Spudich *et al.*, 1995; McLeod *et al.*, 1998; Spillman *et al.*, 1998; Takeo, 1998) considered rotational motions excited by a distant seismic source. A first contribution was a simulation study of rotational effects by Bouchon and Aki (1982), who simulated rotational ground motions near earthquake faults buried in layered media for strike-slip and dip-slip fault models and obtained a maximum rota-

tional velocity of 1.5×10^{-3} rad/sec produced by a buried 30 km long strike-slip fault with slip of 1 m (seismic moment of 8×10^{18} N m). Such small rotational motions are difficult to measure.

Deployment of strong-motion accelerographs in many seismic areas of the world during the past decades has produced data on translational components of motion during many strong earthquakes. These data describe strong motion in three orthogonal directions (two horizontal and one vertical), but because the spacing of the recording sites is much larger than the wavelengths of the recorded motions, little is known today about the accompanying differential and rotational motions in most areas of the world except some rare studies (e.g., Spudich *et al.*, 1995; Huang, 2003; Spudich and Fletcher, 2008).

In recent decades ring laser technology succeeded in detecting weak rotational motions radiated by earthquakes (McLeod *et al.*, 1998; Pancha *et al.*, 2000; Igel *et al.*, 2005; Cochard *et al.*, 2006; Igel *et al.*, 2007). At teleseismic distances the seismic-wave field can be well approximated by plane waves. For example, let us assume a transverse plane wave described by displacement $\mathbf{u} = [0, u_y(t - x/c), 0]$ propagating at phase velocity c. It can be shown using equation (1) that the associated rotation rate is $\Omega_z(x, t) = -(2c)^{-1}\ddot{u}_y(t - x/c)$ (Igel *et al.*, 2005). Therefore, under the plane-wave assumption, rotation rate and transverse acceleration are in phase at any time and the amplitudes are related by

$$\ddot{u}_y(x, t)/\Omega_z(x, t) = -2c. \tag{2}$$

Igel *et al.* (2005) studied the similarity between the colocated translations and rotations recorded by the ring laser. Their observations (over the frequency range 1–150 sec) showed that the waveforms have the expected similarity, and that the amplitude ratios allow an accurate estimate of horizontal phase velocities (Igel *et al.*, 2005; Cochard *et al.*, 2006; Igel *et al.*, 2007). However, in the near-source region, the fundamental assumption of the aforementioned study—plane-wave propagation—might be violated.

Translational and rotational components of strong motion radiated from an earthquake source are modified along the propagation path through interference, focusing, scattering, and diffraction phenomena. In this article, we investigate how ground rotation rates vary for a given slip history and varying hypocenter location, as well as for fixed hypocenter location and varying slip history. We perform numerical modeling considering realistic a quasi-dynamic source and 3D velocity models for the frequency range up to 0.5 Hz and compare with the corresponding effects on translations.

Numerical Green's Functions

In the following, we describe the basic concept of the numerical Green's functions (NGFs) approach, which is based on the discretization of the representation theorem (e.g., Aki and Richards, 2002; Spudich and Xu, 2003; Wang *et al.*, 2008). A target fault plane is divided into equal-sized rectangular subfaults and for each of these subfaults, the corresponding ground response, denoted as NGF, is calculated using a double-couple source mechanism (pure strike slip) with an impulselike slip velocity function. Then, a finite-source scenario can be synthesized by superposition of these NGFs convolved with appropriate slip functions. The method is equivalent to that used, for example, in the COMPSYN code (Spudich and Xu, 2003), which, however, assumes only a 1D medium. More detailed information about our method can be found in Wang (2007) and Wang *et al.* (2008, equations 1 to 4). The forward calculations can be carried out using any numerical solution to the 3D wave propagation problem. Here, we employ a high-order (fourth order in space, second order in time) staggered-grid finite-difference approach (e.g., Igel *et al.*, 1995; Graves, 1996; Ewald *et al.*, 2006) with efficient absorbing boundaries using perfectly matched layers (e.g., Collino and Tsogka, 2001; Marcinkovich and Olsen, 2003) and averaging of elastic moduli and densities to avoid diffraction effects (Moczo *et al.*, 2002). The components of the vector of rotation are extracted by calculating half the curl of the wave field at the surface (equation 1).

We apply the NGF method to the Newport–Inglewood (NI) fault system located in the Los Angeles (LA) basin (Fig. 1). A domain of $96 \times 87 \times 25.5$ km, in the two horizontal and vertical directions, is selected as the study area, being rotated in order to have the x axis parallel to the NI fault. The velocity model is based on the elastic part of the Southern California Earthquake Center (SCEC) 3D velocity model for the LA basin (version 3, Kohler *et al.*, 2003), not considering the inelastic attenuation. The depth of a shear-wave velocity isosurface, 2.0 km/sec, is shown in Figure 2. To reduce the computational effort and the size of the database, we truncate the seismic velocities at 1.4 km/sec, which gives a maximum frequency resolution of 0.56 Hz with our grid spacing of 0.3 km (Wang *et al.*, 2008). Note that such a maximum frequency makes our study relevant, from the engineering point of view, to rather large-scale structures (bridges, etc.). For other structures higher frequencies would be necessary, but we are limited by the computational demand. Moreover, for frequencies larger than, say, 1 Hz the medium model is not detailed enough and some stochastic modeling approach would have to be adopted.

The NI fault is chosen for several reasons: it hosted the M 6.4 Long Beach earthquake in 1933 (Hauksson and Gross, 1991), causing serious damage in LA, and it is still considered the most probable source for a damaging M 7 earthquake in the LA area (Toppozada *et al.*, 1989). The near-vertical plane can be approximated by a vertical plane in the numerical calculation, and the predominant right-lateral slip can be approximated with a pure strike-slip mechanism (Grant and Shearer, 2004). The seismic radiation, which is expected to be sensitive to geometric complexity, is in this case of relatively mature fault well approximated with

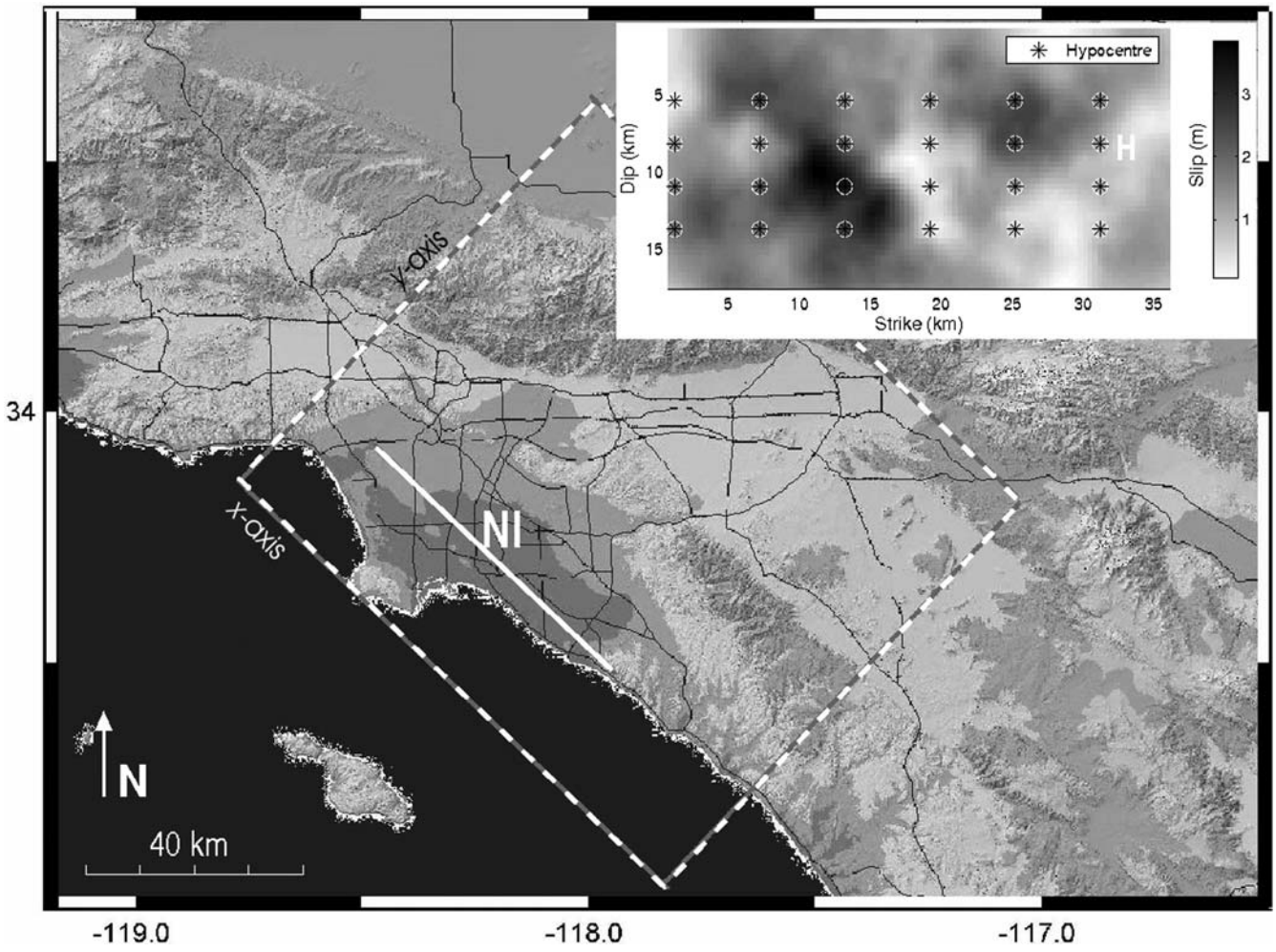

Figure 1. LA area with modeling region (rectangle) and the idealized NI fault. Inset: An example of a final slip distribution of an M 7 earthquake on the vertical NI fault plane and hypocenter grid (asterisks are for the investigation of hypocentral effect on ground motion). H is one such hypocenter, as referred to later in the text.

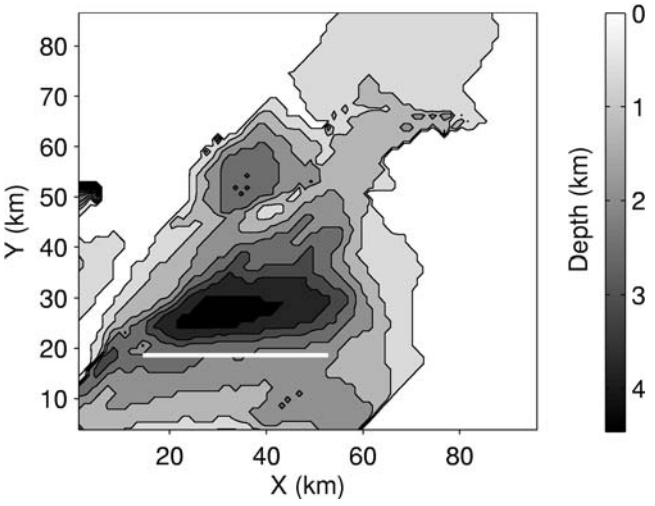

Figure 2. Depth of the 2 km/sec shear-wave velocity isosurface (gray scale). The thick white line indicates the fault trace of the M 7 scenario earthquakes.

a plane-fault assumption (Gallovič *et al.*, 2008; Käser and Gallovič, 2008).

First, as done for the velocity part of ground motion by Wang *et al.* (2008), we determine the fault discretization that provides sufficiently accurate synthetics. The computational setup and source parameters are given in Table 1. The spatial extent of the hypothetical M 7 earthquake fault is obtained

Table 1
Setup for the Finite-Difference Modeling in the LA Basin

Parameter	Value
Spatial discretization (km)	0.3
Time step (sec)	0.018
Lowest S-wave velocity (km/sec)	1.4
Simulation time (sec)	65
Number of cells	$320 \times 350 \times 100$
Perfectly matched layer nodes	15
Fault area (km^2)	18×36
Top depth (km)	1.5

from the source-scaling relation by Wells and Coppersmith (1994). The fault length L and width W equal 36 and 18 km, respectively. The continuous solution has 120×60 subfaults of side 0.3 km, which corresponds to the grid minimum distance in the finite difference (FD) mesh.

The quasi-dynamic rupture process is calculated according to the method published in Guatteri *et al.* (2004). In this model the rupture evolution (including slip velocities) is determined from a given realization of random slip distribution described by a 2D Gaussian autocorrelation function. In our case we use an isotropic correlation length of 5 km for both the strike and dip directions. An example of a realization of such a final slip distribution is shown in the inset of Figure 1. Following Guatteri *et al.* (2004), from the given slip distribution, we compute the static stress change and use a scaling relation to constrain the temporal rupture evolution in terms of nonconstant rupture times and rise times. In this way, the slip evolution to some extent correlates with the slip and the stress drop.

An M 7 finite-fault earthquake scenario is first simulated with all the 120×60 subfaults (treated as the continuous solution). As the ground motions are to be synthesized for a huge number of receivers spanning the whole surface of the computational domain, we seek the coarsest fault discretization in order to save some computational time. The ground rotation rates are then synthesized from a coarser fault discretization (namely 5×5 and 6×6 FD grid points) and compared to the continuous solution. Figure 3 shows the results of the verification. The z component of rotation rate has much larger amplitude (and error) than the other two components (not shown) because of the pure strike-slip source mechanism and, thus, is used to illustrate the results. The peak ground rotation rates (PGRRs), or, alternatively, peak ground rotational velocity, covering frequencies up to 0.5 Hz for different source discretizations are compared over the entire study area. Figure 3a shows spatial (map) distribution of the relative PGRR difference, that is, the difference between PGRRs for a discretized solution and the continuous one divided by the PGRR of the continuous solution. The largest relative difference is only 18% at the point denoted as P1 in the figure. In fact, the waveforms for different discretizations are almost identical as can also be seen from the waveform comparison (Fig. 3b) for point P1, where the largest relative PGRR difference is observed. Additionally, Figure 3c compares waveforms for different discretizations along the UV profile (see Fig. 3a). The lowest correlation coefficient value is 0.991. In conclusion, we further use solutions with 1.5 km subfault side-length (5×5 FD grid points) as they are accurate enough for the M 7 scenario earthquakes under study. This information might also be useful for other modelers as they can compute the Green's functions for only the coarse discretization and save some computational time (our preferred discretization requires approximately twenty-five times less computational time with respect to the continuous solution). However, attention has to be paid because the fault discretization required depends on rupture velocity, maximum frequency considered, etc. (Wang *et al.*, 2008).

Earthquake Scenario Simulations

The precalculated NGF database allows us—within the limits of the method (e.g., reliable frequency range)—to synthesize ground motions from arbitrary strike-slip histories on the NI fault for the complete study area. How variations of the source parameters (namely hypocenter location and slip distributions) influence the shaking for a scenario earthquake is important for the estimation of seismic hazard. This is the question we will focus on in this study for the potential case of an M 7 earthquake on the NI fault. As discussed previously, we use the quasi-dynamic source model (Guatteri *et al.*, 2004) and the SCEC 3D velocity model for the LA basin. The aim is to investigate the composite effect of the 3D structure and the source complexity on the ground rotation rates and to provide a possible range of the ground rotation rates that might be generated by an M 7 earthquake on the NI fault. The results are shown and analyzed in the following sections.

Effect Due to Hypocenter Location

In this section, we investigate how variations of the hypocenter location for a given final slip distribution influence the ground rotation rate. Mai *et al.* (2005) studied statistically the relation between the nucleation point positions and the inverted slip models, showing that the hypocenters lie predominantly close to the large-slip asperities. Nevertheless, to keep our study systematic and to include even the, perhaps, less plausible models with hypocenters lying further from the asperities, we assume a regular grid of 4×6 hypocenters in the seismogenic zone (5–15 km depth) as indicated in the inset of Figure 1. The nucleation point together with the considered slip distribution constrain all the remaining kinematic features of the source model (rise times, rupture times, etc.). For each of these source models six-component seismograms are synthesized using the NGF database for the entire surface grid of receivers and analyzed. Only the PGRRs are discussed.

In Figure 4 we show maps of ground rotation rate due to varying hypocenter location in terms of maximum ground rotation rates and their variations. The maximum values describe how fast a station could rotate during scenario M 7 earthquakes. In this study we aim to quantify the variations of ground rotation characteristics due to source characteristics. To this end, two ratios are considered: R_{SD}—standard deviation relative to mean value, and R_{max}—maximum value divided by mean value. R_{max} quantifies the expected variations in specific regions.

At first glance, all the maps in Figure 4 exhibit complex patterns. The largest rotation rate of the entire study area for the vertical component is eight times larger than those of the x component and five times larger than those of the y com-

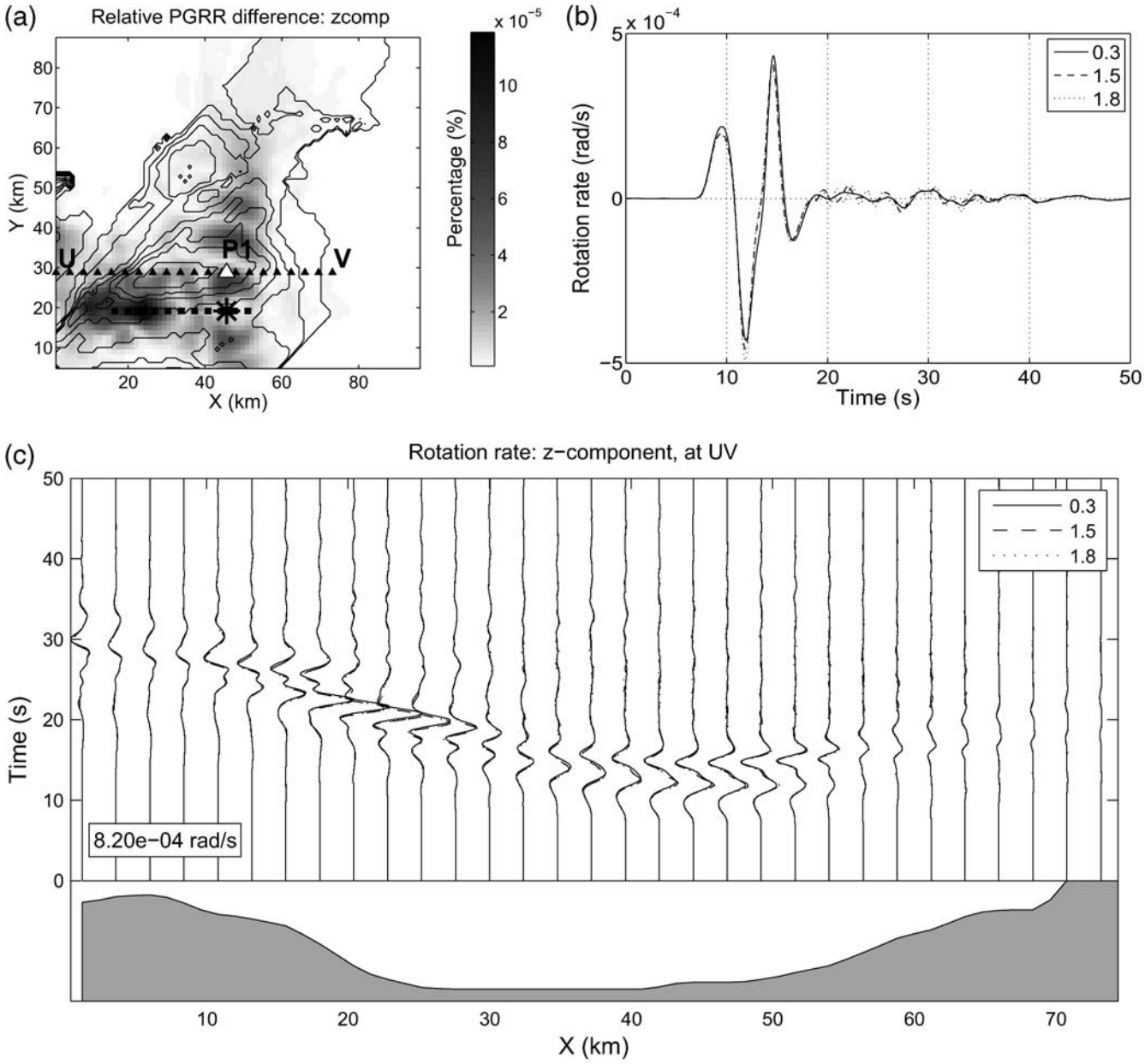

Figure 3. Effect of fault discretization on rotation rate. (a) PGRR difference (z component) between the solution for the 1.8 km subfault size and the continuous solution (subfault size of 0.3 km, corresponding to the finite-difference grid step). The dashed thick white line marks the fault trace and the white asterisk shows the epicenter. (b) Rotation rate seismograms (z component) from different solutions (subfault sizes of 0.3 km, 1.5 km, and 1.8 km) at receiver P1 (largest misfit). (c) Rotation rate profile along UV (see panel a) in which the depth of the shear-wave velocity isosurface at 2.0 km/sec is shown at the bottom. The largest rotation rate amplitude across this profile is shown (inset).

ponent. This phenomenon can be attributed to the source mechanism (pure strike slip). One can also see the amplification at all components in the basin area due to the lower wave velocities. The maximum rotation rate over the entire study area is observed close to the fault trace (inside region A surrounding the fault trace) but at varying places for different components. In region A for the x component, the maximum PGRR distribution is quite symmetrical about the middle of the fault trace in the x direction (Fig. 4, top left-hand panel). This symmetry is observed to a lesser extent for the other two components (Fig. 4, middle and bottom left-hand panels).

The ground-motion variation due to varying hypocenters is illustrated by showing the spatial distribution of the R_{SD} ratio (Fig. 4, middle column). We focus on the two regions B and C, where substantial basin depth variations are located, to illustrate the 3D effect on rotations. For the x component, there is no noticeable high R_{SD} (Fig. 4, top middle panel) inside these two regions. However, for the y component (Fig. 4, center panel) and the z-component (Fig. 4, bottom middle panel), a large R_{SD} is observed when compared to the neighboring areas. The largest R_{SD} of the whole study area, 75% for the y component and 72% for the z component, are all

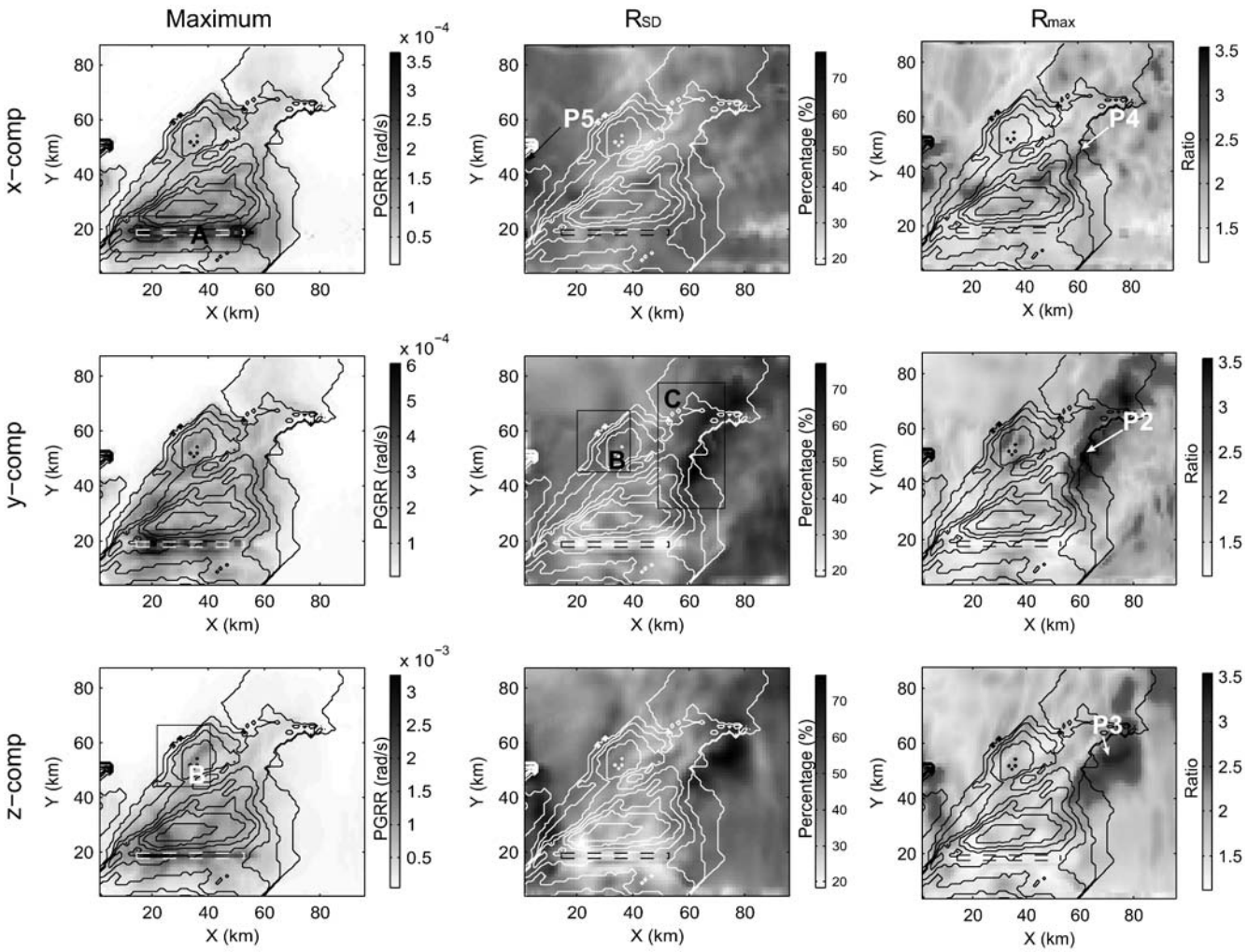

Figure 4. PGRR maps and their variability when using 24 hypocenter positions (see inset in Fig. 1). Left-hand column: maximum value. Middle column: R_{SD} (ratio between the standard deviation and the mean PGRR value). Right-hand column: R_{max} (ratio between the maximum value and the mean value). From the top to bottom row are the *x*, *y*, and *z* components, respectively. The black dashed rectangle is used to indicate the fault trace in order to avoid masking the high values on the fault trace. Thin white lines are contours of the 2 km/sec shear velocity isosurface. Regions A, B, and C and stations P2, P3, P4, and P5 are indicated for discussion in the text. Note the scale difference for the maximum values (left-hand column) between the horizontal and vertical components.

located inside region C. Right on the fault trace, the R_{SD} ratio for the *x* component (Fig. 4, top middle panel) is similar to that in the neighboring regions. On the contrary, for the other two components (Fig. 4, center panel and bottom middle panel) the values above and close to the fault are smaller than those further from the fault. For all three components, but especially for the *z* component, large R_{SD} values are found in the regions off both tips of the fault trace.

The distributions of the R_{max} ratio are shown in Figure 4 (right-hand column). For the *y* and *z* components (Fig. 4, middle and bottom right-hand panels), large values are observed in regions B (small basin) and C (i.e., same as for R_{SD}). Moreover, the largest R_{max} over the entire study area lies at the same positions (P2 for the *y* component and P3 for the *z* component) as for the R_{SD} case. Small values are observed near the fault plane (region A) when compared to the neighboring areas. For the *x* component, the largest R_{max} is at station P4, whereas the largest R_{SD} is at station P5. At some places, the rotation rates can be two to three times larger than the mean rotation rates, which applies to all components.

To summarize, generally, the largest values occur for the vertical rotational components. Maxima of all the components are concentrated in the basin area. For the *x* component, the largest values are close to the tips of the fault, which suggests that this component is mostly sensitive to the sole source (directivity) effect. The other two components are affected by a combination of the source and basin effects as the largest variations are located close to the basin edge (region C in Fig. 4).

Effect Due to Slip Distribution

Here, we study the effect of the slip distribution keeping the hypocenter constant. We generate 20 random slip distri-

butions, each corresponding to an M 7 earthquake. Again the other kinematic parameters are obtained by the use of the quasi-dynamic approach by Guatteri *et al.* (2004).

The results are shown in Figure 5 in the same way as in Figure 4. As in the previous case, the mapped quantities exhibit complex behavior. The largest rotation rate of the entire study area for the vertical component is 4.5 times larger than those of the x component and 6 times larger than those of the y component. For the x and z components (Fig. 5, top and bottom left-hand panels), the largest rotation rates are located above the fault, further from the epicenter close to the far right-hand end of the fault trace (region E). For the y component, the largest rotation rates happen at distinct points above the fault but also further from the fault trace (point P6 in Fig. 5, middle left-hand panel). For the x and z components, the rotation rates around point P6 are much smaller than those on the fault trace.

The spatial distributions of R_{SD} for all 20 simulations are shown in Figure 5, middle column. The largest R_{SD}s of the entire study area are similar for all components (42% for the x component, 50% for the y component, and 45% for the vertical component) but not located at the same places. For the x component, R_{SD} is very large inside region F, which is around the epicenter. For the other two components, the high ratios are restricted inside region G (banded region perpendicular to the fault trace). At point P7 (small basin edge), higher ratios are found for the y and z components but not for the x component when compared to those areas around the fault trace (region F). Right above the fault, varying slip distributions introduce more variations on the fault-parallel component of the rotation rate than on the other two components.

The spatial distributions of the R_{max} ratio are shown in Figure 5, right-hand column. These distributions are quite similar to those for R_{SD}: the largest values of the entire study area are observed in the same areas. Right above the fault, large R_{max} values are observed for the x component but not for the other two components, for which large values of R_{max}

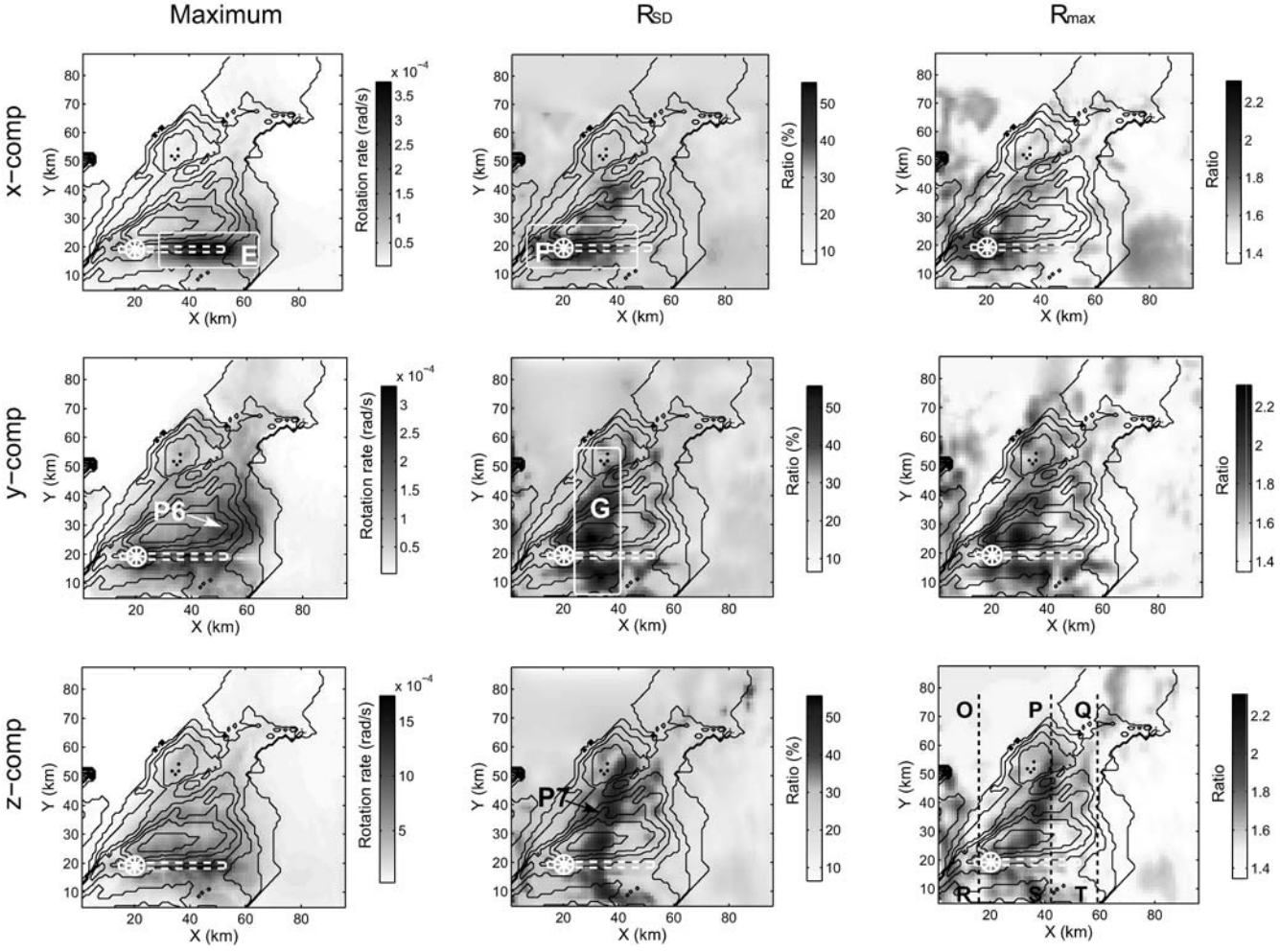

Figure 5. Same as Figure 4 but for random variations of the slip history with a fixed hypocenter (epicenter indicated by the wheel symbol). Regions E, F, and G, stations P6 and P7, and profiles OR, PS, and QT are indicated for discussion in the text. Note the scale difference for the maximum values (left-hand column) between the horizontal and vertical components.

are mostly restricted to region G (banded region perpendicular to the fault trace) further from the fault. High R_{max} values are observed at point P7 (basin edge) for the z component.

Let us compare results obtained for a varied hypocenter position (Fig. 4). The distribution of maximum values (Figs. 4 and 5, left-hand columns) are very similar because the maxima are located within the basin and close to the fault. Comparing the results shown in Figures 4 and 5 in terms of R_{SD} and R_{max} (middle and right-hand columns), we can observe that varying the hypocenter has a stronger effect than keeping the hypocenter fixed and varying the slip histories. The case of varying slip distribution is characterized by larger variations within the basin in contrast to the case of varying hypocenter positions, for which the largest variations are located at the borders (y and z components) or outside (x component) of the basin.

Comparison with Translations

For a horizontally polarized plane wave, the horizontal (transverse) acceleration and the vertical rotation rate have identical waveforms; they are scaled by twice the phase velocity, see equation (2) (e.g., Igel *et al.*, 2005, 2007). Comparison of synthetic vertical rotation rates and horizontal accelerations simulated for the M 7 hypothetical earthquakes on the NI fault showed that wavefronts are (near) planar (Wang, 2007) and that it is appropriate to relate peak amplitudes of translations and rotations. Because this amplitude ratio is related to the local phase velocity (equation 2), the ratios should be smaller inside the basin than outside because the basin is characterized by lower velocities. Note that we do not expect perfect match with the medium velocities because (1) the plane-wave assumption is not perfectly satisfied and (2) the medium has depth-dependent velocities so only some mean velocity can be obtained. We denote mean value of the peak ground accelerations as M_{PGAx} and M_{PGAy} for the x and y components, respectively. The mean value of the peak vertical rotation rate is denoted as M_{PGRRz}.

Figure 6 shows the ratios M_{PGAx}/M_{PGRRz} and M_{PGAy}/M_{PGRRz} in map view (omitting the factor 2), together with the basin depth (isosurface of the 2 km/sec shear-wave velocity), for the cases of varying hypocenter (left-hand column) and varying slip history (right-hand column). For the x component of acceleration (Fig. 6, top row) the ratios are small inside the basin. Outside of the basin, except for region I, the estimated ratio is higher. In region I the ratio is still low, which is not in agreement with the larger velocities therein. This is not surprising because the waveforms themselves are not expected to be similar for the x component (propagation direction). In regions close to the northwest tip of the fault trace, when varying either hypocenter location or slip history (Fig. 6, top row), the ratio is distinctly larger than 4000 m/sec, being much larger than those in the neighboring areas and not compatible with the velocity model. In such areas, however, the assumption of an incoming plane wave is roughly violated.

For the y component of acceleration (Fig. 6, middle row), in region J (being outside the basin and thus characterized by large velocities) the ratio between the acceleration and the vertical rotation rate is less than 1700 m/sec for the varying hypocenter case (Fig. 6, middle left-hand panel). This is, however, too low a value for the area outside of the basin. We explain this due to poor similarity of the y component of acceleration and the vertical rotation rate waveforms in this area (Wang, 2007). In the strike directions where the correlations are better, the predicted ratios are larger, corresponding to larger velocities outside the basin. For the varying slip history case (Fig. 6, middle right-hand panel), the ratios in region J are higher (corresponding to higher velocities in that area), which is, however, perhaps only accidental, because in region K (above the fault) the ratios are again higher than what would correspond to the local velocities. On the other hand, off the fault in the strike direction, the ratios again correspond roughly to the velocity model.

A map of the average between the two ratios discussed previously, $1/2(M_{PGAx} + M_{PGAy})/M_{PGRRz}$, is shown in Figure 6 (bottom row) for both varying the hypocenter (bottom left-hand panel) and varying the slip history (bottom right-hand panel). A strong relation between this average and the local velocity is observed over almost the entire study area in these two cases. Large values of this parameter nicely delineate the basin structure. The only exceptions are the small regions around the tips of the fault trace where the plane-wave assumption is clearly violated.

Decay with Distance

It is of practical importance to study how the peak rotation rates decay with distance. In particular, one can ask to what extent is the decay comparable to the decay known for peak translation motion (peak ground acceleration, peak ground velocity, etc.), which is usually characterized by the attenuation relations.

In Figure 7 we show the maximum amplitude of both the y component of acceleration and the vertical rotation rate synthesized for the case of varying the hypocenter location and plot them against the distance to the fault. At first glance, the shapes of the point clouds are very similar. Both the acceleration and the rotation rate saturate for fault distances less than 10 km. It is also seen that the mean rotation rate decreases with fault distance similarly to acceleration for fault distances larger than 10 km. Local increase of the largest values is observed for both the rotation rates and the accelerations within range L (between 25 and 53 km). It covers the small basin depicted as region B and the steepest basin edge in region C in Figure 4, suggesting that the rotation rates are amplified in a way similar to acceleration by the small basin and the basin edge.

In conclusion, rotation rate linearly decreases with fault distance in log–log coordinates just as acceleration does. This suggests that when developing attenuation relationships

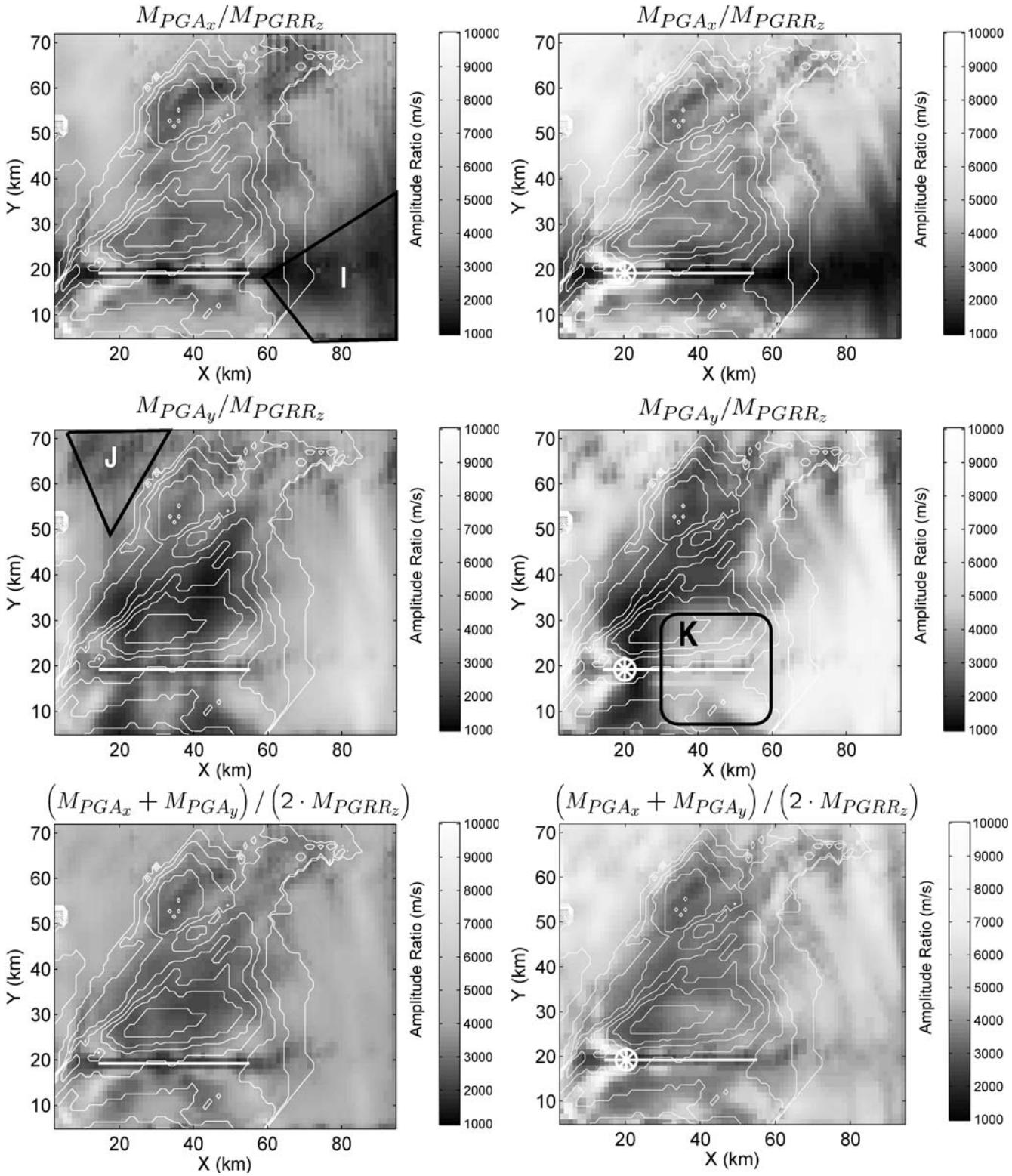

Figure 6. Maps of ratios between peak acceleration and peak rotation rate (*z* component). Left-hand column: varying hypocenter. Right-hand column: varying slip history. Top row: acceleration, *x* component. Middle row : acceleration, *y* component. Bottom row: geometric mean of the two horizontal accelerations. Black curved lines mark the contours of the 2.0 km/sec shear-wave velocity isosurface. The red asterisk marks the epicenter for the case of varying slip history. The white line marks the fault trace. Regions I, J, and K are indicated for discussion in the text.

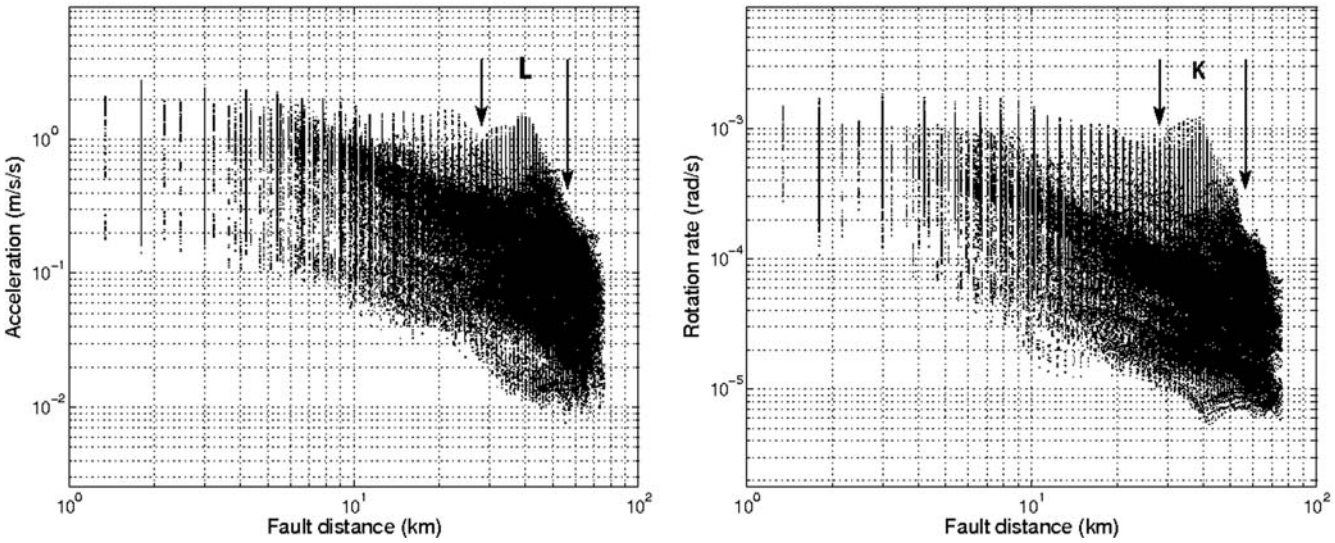

Figure 7. Comparison of peak ground accelerations and PGRRs as a function of distance to the fault when varying hypocenter location. Left-hand panel: *y* component of acceleration. Right-hand panel: *z* component of rotation rate. Fault distance range denoted as *L* is shown for discussion in the text.

for rotational motions, similar expressions (as a function of distance) as for the peak acceleration can be adopted.

Discussion and Conclusions

We investigated how rupture-model variability and 3D structure affect ground rotation rates in the frequency range up to 0.5 Hz. In the region surrounding the fault trace, the vertical component of rotation rates is systematically several times larger than the other two horizontal components, showing that the source mechanism (pure strike slip) dominates the ground rotation rates in this region.

Variation in the hypocenter location leads to large variations of the ground rotation rates. The fault-perpendicular component of acceleration and the vertical rotation rates are strongly affected by both the medium (basin structure) and the slip asperity location. However, there are no obvious effects of either the medium or the slip asperity location on the fault-parallel component. That component is dominated by the directivity effect. The basin effect is also observed for the variations of the *y* and *z* components of the peak rotation rates, the largest variations being located at the basin edges. In the region close to the fault, where large rotation rates are observed, the variations are small. Hence, not only the hypocenter location but also the elastic properties of the medium control the rotation rate variations.

For the case of varying slip history, the directivity effect (if present) dominates the fault-parallel component in terms of absolute values and relative variations. These variations are, however, smaller than those for the case of varying hypocenter location. The velocity medium effect is mainly pronounced on the fault-perpendicular component when considering the maximum value. The variations of the rotation rates are largest in the basin structure, especially for the *y* and *z* components.

Vertical rotation rates can be compared to horizontal accelerations as was done on the global scale by Igel *et al.* (2005, 2007). These authors theoretically derived, assuming plane-wave incidence, the relation between the horizontal accelerations and vertical rotation rates. The waveforms are very similar, scaled by twice the local phase velocity (see equation 2). In our study, we have found areas where the waveform of one component of the horizontal acceleration was very similar to the vertical rotation rate waveform (Wang, 2007). This is consistent with the shear-wave radiation pattern of a double couple. The fault-parallel component of acceleration is similar to the vertical rotation rate in areas perpendicular to the fault strike, while the fault-normal component of acceleration is highly correlated to the vertical rotation rate in the strike direction of the fault. Therefore, waveform similarity is observed over the entire study area for at least one of the acceleration horizontal components. When the average of these ratios is considered, a good agreement is obtained over the whole area under study. We have found good correlation with the velocity model except for a very small region surrounding the fault trace. This suggests a new tool for basin edge detection based on the coprocessing of translational and rotational ground motion. This, of course, would require development of portable rotation meters and systematic surveys of an area under study.

Finally, vertical rotation rate is found to decay with distance in a way very similar to acceleration. Therefore, similar expressions (as a function of distance) as peak acceleration can be adopted for rotational motions attenuation relationships. This result is supported by the recent findings of Stupazzini *et al.* (2009).

Data and Resources

The synthetic data used in this study were generated entirely using a 3D finite-difference code (Ewald *et al.*, 2006) implemented in parallel on the supercomputers of the Leibniz Supercomputer Centre in Munich, Germany. Information on the LA basin velocity model (Kohler *et al.*, 2003) was obtained from the SCEC web site (www.scec.org).

Acknowledgments

This work was partially funded by the International Quality Network-Georisk (German Academic Exchange Service) and the Elite Graduate College THESIS (elite.geophysik.uni-muenchen.de). F. G. has been supported by the Grant Agency of the Czech Republic (Grant Number 205/08/P013) and Grant Number MSM0021620800. We also acknowledge support from the European Human Resources Mobility Programme (Research Training Network SPICE, www.spice-rtn.org) and the provision of computational resources through the Leibniz Computing Centre Munich. We thank Martin Mai and one anonymous reviewer for excellent comments. We also thank KONWIHR for their support.

References

Aki, K., and P. G. Richards (2002). *Quantitative Seismology*, Second Edition, University Science Books, New York.

Boratynski, W., and R. Teisseyre (2004). Generalized continuum with defects and asymmetric stresses, *Acta Geophys. Pol.* **52,** 185–195.

Bouchon, M., and K. Aki (1982). Strain, tilt, and rotation associated with strong ground motion in the vicinity of earthquake faults, *Bull. Seismol. Soc. Am.* **72,** 1717–1738.

Cochard, A., H. Igel, A. Flaws, B. Schuberth, J. Wassermann, and W. Suryanto (2006). Rotational motions in seismology, in *Earthquake Source Asymmetry, Structural Media and Rotation Effects*, R. Teisseyre, M. Takeo, and E. Majewski (Editors), Springer-Verlag, New York, 391–412.

Collino, F., and C. Tsogka (2001). Application of the PML absorbing layer model to the linear elastodynamic problem in anisotropic heterogeneous media, *Geophysics* **66,** 294–307.

Ewald, M., H. Igel, K. G. Hinzen, and F. Scherbaum (2006). Basin-related effects on ground motion for earthquake scenarios in the Lower Rhine Embayment, *Geophys. J. Int.* **166,** 197–212.

Gallovič, F., M. Käser, J. Burjánek, and Ch. Papaiannou (2008). 3-D modeling of near-fault ground motions of the 2004 Parkfield earthquake with non-planar rupture models and topography, *J. Geophys. Res.* (in press).

Grant, L. B., and P. M. Shearer (2004). Activity of the offshore Newport–Inglewood Rose Canyon fault zone, coastal southern California, from relocated microseismicity, *Bull. Seismol. Soc. Am.* **94,** 747–752.

Graves, R. W. (1996). Simulating seismic wave propagation in 3D elastic media using staggered grid finite differences, *Bull. Seismol. Soc. Am.* **86,** 1091–1106.

Guatteri, M., P. M. Mai, and G. C. Beroza (2004). A pseudo-dynamic approximation to dynamic rupture models for strong ground motion prediction, *Bull. Seismol. Soc. Am.* **94,** 2051–2063.

Gupta, I. D., and M. D. Trifunac (1987). Statistical analysis of response spectra method in earthquake engineering, Dept. of Civil Engineering, Univ. of Southern California, Los Angeles, California, report.

Gupta, I. D., and M. D. Trifunac (1988). A note on computing the contribution of rocking excitation to earthquake response of simple buildings, *Bull. Indian Soc. Earthq. Tech.* **25,** 2, 73–89.

Gupta, I. D., and M. D. Trifunac (1990). Probabilistic spectrum superposition for response analysis including the effects of soil-structure interaction, *J. Probab. Eng. Mech.* **5,** 9–18.

Gupta, V. K., and M. D. Trifunac (1989). Investigation of building response to translational and rotational earthquake excitations, Dept. of Civil Engineering, Univ. of Southern California, Los Angeles California, report.

Gupta, V. K., and M. D. Trifunac (1991). Effects of ground rocking on dynamic response of multistoried buildings during earthquakes, *Proc. JSCE Struct. Eng. Earthq. Eng.* **8,** no. 2, 43–50.

Hauksson, E., and S. Gross (1991). Source parameters of the 1933 Long Beach earthquake, *Bull. Seismol. Soc. Am.* **81,** 81–98.

Huang, B. S. (2003). Ground rotational motions of the 1999 Chi-Chi, Taiwan, earthquake as inferred from dense array observations, *Geophys. Res. Lett.* **30,** 1307–1310.

Igel, H., A. Cochard, J. Wassermann, A. Flaws, U. Schreiber, A. Velikoseltsev, and N. Pham Dinh (2007). Broad-band observations of earthquake-induced rotational ground motions, *Geophys. J. Int.* **168,** 182–197.

Igel, H., P. Mora, and B. Riollet (1995). Anisotropic wave propagation through finite-difference grids, *Geophysics* **60,** 1203–1216.

Igel, H., U. Schreiber, A. Flaws, B. Schuberth, A. Velikoseltsev, and A. Cochard (2005). Rotational motions induced by the *M* 8.1 Tokachi-oki earthquake, September 25, 2003, *Geophys. Res. Lett.* **32**.

Käser, M., and F. Gallovič (2008). Effects of complicated 3D rupture geometries on earthquake ground motion and their implications: a numerical study, *Geophys. J. Int.* **172,** 276–292.

Kohler, M., H. Magistrale, and R. Clayton (2003). Mantle heterogeneities and the SCEC three-dimensional seismic velocity model version 3, *Bull. Seismol. Soc. Am.* **93,** 757–774.

Mai, P. M., P. Spudich, and J. Boatwright (2005). Hypocenter locations in finite-source rupture models, *Bull. Seismol. Soc. Am.* **95,** no. 3, 965–980.

Marcinkovich, C., and K. B. Olsen (2003). On the implementation of perfectly matched layers in a 3D fourth-order velocity-stress finite-difference scheme, *J. Geophys . Res.* **108,** 2276–2293.

McLeod, D. P., G. E. Stedman, T. H. Webb, and U. Schreiber (1998). Comparison of standard and ring laser rotational seismograms, *Bull. Seismol. Soc. Am.* **88,** 1495–1503.

Moczo, P., J. Kristek, V. Vavrycuk, R. J. Archuleta, and L. Halada (2002). 3D heterogeneous staggered-grid finite-difference modeling of seismic motion with volume harmonic and arithmetic averaging of elastic moduli and densities, *Bull. Seismol. Soc. Am.* **92,** no. 8, 3042–3066.

Newmark, N. M., and H. J. Hall (1969). Seismic design criteria for nuclear reactor facilities, *Proc. of the 4th World Conf. on Earthquake Engineering* Santiago, Chile.

Newmark, N. M., and E. Rosenblueth (1971). *Fundamentals of Earthquake Engineering* Prentice Hall, New York.

Nigbor, R. L. (1994). Six-degree-of-freedom ground-motion measurement, *Bull. Seismol. Soc. Am.* **84,** 1665–1669.

Pancha, A., T. H. Webb, G. E. Stedman, D. P. McLeod, and U. Schreiber (2000). Ring laser detection of rotations from teleseismic waves, *Geophys. Res. Lett.* **27,** 3553–3556.

Spillman, W. B., D. R. Huston, and J. Wu (1998). Very long gauge length fiber optic seismic event detectors, *Proc. SPIE* **3555,** 311–321.

Spudich, P., and J. B. Fletcher (2008). Observation and prediction of dynamic ground strains, tilts and torsions caused by the *M* 6.0 2004 Parkfield, California, earthquake and aftershocks derived from UPSAR array observations, *Bull. Seismol. Soc. Am.* **98,** no. 4, 1898–1914, doi 10.1785/0120070157.

Spudich, P., and L. Xu (2003). Software for calculating earthquake ground motions from finite faults in vertically varying media, *IASPEI Handbook of Earthquake and Engineering Seismology, Part B*, Academic, New York, 1633–1634 (with associated software on accompanying CD).

Spudich, P., L. K. Stek, M. Hellweg, J. B. Fletcher, and L. M. Baker (1995). Transient stresses at Parkfield, California, produced by the *M* 7.4 Landers earthquake of June 28, 1992: observations from the UPSAR dense seismograph array, *J. Geophys. Res.* **100,** 675–690.

Stupazzini, M., J. de la Puente, C. Smerzini, M. Käser, H. Igel, and A. Castellani (2009). Study of rotational ground motion in the near-field region, *Bull. Seismol. Soc. Am.* **99,** no. 2B, 1271–1286.

Takeo, M. (1998). Ground rotational motions recorded in near-source region of earthquakes, *Geophys. Res. Lett.* **25,** 789–792.

Teisseyre, R. (2004). Spin and twist motions in a homogeneous elastic continuum and crossband geometry of fracturing, *Acta Geophys. Pol.* **52,** 173–183.

Toppozada, T. R., J. H. Bennett, G. Borchardt, R. Saul, and J. F. Davis (1989). Earthquake planning scenario for a major earthquake on the Newport–Inglewood fault zone, *Calif. Geol.* **42,** no. 4.

Wang, H. J. (2007). Source-dependent variations of *M* 7 earthquakes in the Los Angeles Basin, *Ph.D. Thesis*, Ludwig-Maximilian-University, http://edoc.ub.uni-muenchen.de/7555.

Wang, H. J., H. Igel, F. Gallovič, A. Cochard, and M. Ewald (2008). Source-related variations of ground motions in 3-D media: application to the Newport–Inglewood fault, Los Angeles Basin, *Geophys. J. Int.* **175,** 202–214, doi 10.1111/j.1365-246X.2008.03878.x.

Wells, D. L., and K. J. Coppersmith (1994). New empirical relationships among magnitude, rupture length, rupture width, rupture area, and surface displacement, *Bull. Seismol. Soc. Am.* **84,** 974–1002.

Yamaguchi, R., and T. Odaka (1974). Field study of the Izu-Hanto-oki earthquake of 1974, *Bull. Earthq. Res. Inst, Tokyo Univ.* **14,** 241–255.

Zembaty, Z. B. (2006). Deriving seismic surface rotations for engineering purposes, in *Earthquake Source Asymmetry Structural Media and Rotation Effects*, Springer-Verlag, New York.

Zembaty, Z., and G. Boffi (1994). Effect of rotational seismic ground motion on dynamic response of slender towers, *Eur. Earthq. Eng.* **8,** 3–11.

Department of Earth and Environmental Studies
Geophysics Section
Ludwig-Maximilians-University
München, Germany
heiner.igel@geophysik.uni-muenchen.de
(H.W., H.I.)

Department of Geophysics
Faculty of Mathematics and Physics
Charles University
Prague, Czech Republic
(F.G.)

Ecole et Observatoire des Sciences de la Terre
5 rue René Descartes
67084 Strasbourg Cedex, France
(A.C.)

Manuscript received 5 June 2008